Journal of
Materials Chemistry A

Accepted Manuscript

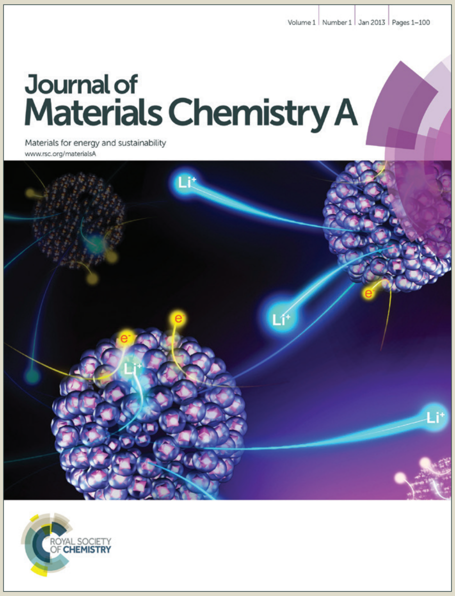

ROYAL SOCIETY
OF CHEMISTRY

www.rsc.org/materialsA

Journal of Materials Chemistry A RSCPublishing

ARTICLE

Cite this: DOI: 10.1039/x0xx00000x

Received ,
Accepted

DOI: 10.1039/x0xx00000x

www.rsc.org/MaterialsA

Electrical properties and flux performance of composite ceramic hydrogen separation membranes

J. S. Fish,[a,b] S. Ricote,[c] R. O'Hayre[b] and N. Bonanos[a]

The electrical properties and hydrogen permeation flux behavior of the all-ceramic protonic/electronic conductor composite $BaCe_{0.2}Zr_{0.7}Y_{0.1}O_{3-\delta}/Sr_{0.95}Ti_{0.9}Nb_{0.1}O_{3-\delta}$ (BCZY27/STN95: BS27) are evaluated. Conductivity and hydrogen permeability are examined as a function of phase volume ratios. Total conductivities of 0.01 – 0.06 $S\cdot cm^{-1}$ are obtained in moist (+ 1 % H_2O) H_2/inert gas from 600 – 800 °C for 50 volume % STN95. With increasing STN95 content (60 and 70 volume %), conductivity increases by 5 – 10 times, but displays a semiconductor-type dependence, even at 70 volume % STN95. The conductivity is modeled with an effective medium approach incorporating a term for the heterojunctions between the two phases. Hydrogen fluxes of 0.004 – 0.008 $\mu mol\cdot cm^{-2}\cdot s^{-1}$ are obtained for a 50 volume % STN95 membrane sample (1 mm thickness) at 600 – 800 °C using dry argon as a sweep gas. Upon adding palladium layers as catalysts more than a five-fold increase is observed in the hydrogen flux, 0.025 – 0.026 $\mu mol\cdot cm^{-2}\cdot s^{-1}$, over the same temperature range. Hydrogen flux is not observed for membranes made from the 60 and 70 % STN95 samples.

Introduction

Mixed-conducting composite membranes are garnering significant attention for use in a variety of energy conversion and storage applications. In high-temperature membrane reactors (700 – 800 °C), such as those required for gas-to-liquid fuel refining, proton-conducting ceramic oxides composited with transition metals (*e.g.*, Ni) are attractive candidates.[1,2] However, it is desirable to replace these ceramic-metal (cermet) composites with ceramic-ceramic (cercer) composites, having similar levels of electronic and protonic conductivity under a wide range of chemical potentials, while eliminating the vulnerability of the metal component to poisoning and passivation. As such, all-ceramic systems can offer decreased cost and improved resistance to corrosive and poisonous environments.[3,4] Membrane compositions involving only earth-abundant elements are a particular focus of recent attention.[5-8]

Among the oxide-based proton conductors, Y-doped $BaZrO_3$ (BZY) and $BaCeO_3$ (BCY) show some of the highest reported proton conductivities and are the most intensely studied.[9] While oxides based on $BaCeO_3$ are vulnerable to decomposition upon exposure to CO_2,[10,11] solid solutions of Y-doped $BaCeO_3$ and $BaZrO_3$ ($BaCe_{1-x-y}Zr_xY_yO_{3-\delta}$, BCZY or BZCY) with $x \geq 0.3$ have demonstrated stability in CO_2-containing atmospheres.[10] While these acceptor-doped perovskites possess protonic and *p*-type electronic (hole) conductivity in oxidizing atmospheres, the *p*-type component becomes negligible under reducing conditions typical of hydrogen separation environments, rendering them ineffective as single-phase hydrogen permeation membranes. For such applications, a single-phase or dual-phase mixed ionic-electronic conductivity membrane material with strong protonic and *n*-type character, as well as high chemical and thermal stability, is required.

The current work investigates the latter case of a composite membrane consisting of two perovskite materials, $BaCe_{0.2}Zr_{0.7}Y_{0.1}O_{3-\delta}$ (BCZY27) as the protonic conductor and Nb-doped Sr-deficient strontium titanate, $Sr_{0.95}Ti_{0.9}Nb_{0.1}O_{3-\delta}$ (STN95) as the *n*-type electronic conductor. The composite is referred to as BS27. The effect of composition on the composite's electrical and permeation transport properties is investigated by varying the fraction of the STN95 phase from 50 – 70 volume %, referred to in the work as BS27_5050, BS27_4060, and BS27_3070. The synthesis and microstructural characterization of BS27 has been published elsewhere.[12] The present work also presents a model for describing the electrical properties of BS27 composites whose parameters are determined by fitting to data for multiple samples of each composition.

Experimental procedures

STN95 and BCZY27 powders were prepared from oxide and carbonate precursors by solid state reaction. Spark plasma sintering (SPS) was used to fabricate dense pellets of the composite for conductivity and hydrogen permeation measurements. Dense composite samples (> 90 % theoretical) were produced by SPS at 1300 – 1350 °C under a 50 MPa load at hold times from 30 s – 5 min. Full details of the synthesis procedures for the composite as well as the pure STN95 and BCZY27 samples are published elsewhere.[12] XRD patterns of the pure materials and a typical BS27_5050 sample are given in the Supplementary Materials.[†] While the SPS process generated highly dense, membrane-quality BS27 samples of each composition, the majority of them cracked after synthesis due to residual stresses during cooling and were unusable for permeation experiments.

Conductivity measurements

BCZY27 and STN95 conductivity samples were made from the same powder batches used to produce the BS27 mixtures. Samples were sintered in chamber and tube furnaces in either air (BCZY27) or reducing atmosphere (STN95). For BCZY27, 1 weight % NiO was mixed with the calcined powder by ball-milling for 24 h. After mixing, disc-shaped pellets of 12 mm ∅ and 2 mm thick were pressed and sintered in air at 1400 °C for 12 h. Platinum paste was painted onto both sintered faces and a final heat treatment was done at 1000 °C for 2 h in air to adhere the electrodes. STN95 samples were pressed as rectangular bars, sintered for 12 h at 1400 °C in 9 % H_2/N_2 humidified by a room-temperature bubbler (+ 3 % H_2O), and subsequently machined into to 4 × 4 × 18 mm dimensions using diamond tools. Platinum wires were wound around the ends of the bars and platinum paste was painted over them to ensure sufficient electrical contact. The electrode wires and paste were fired at 1100 °C for 2 h in dry 9 % H_2/N_2 to maintain the sample's reduced state.

BS27 composite samples for conductivity testing were prepared as square pellets ca. 5 – 7 mm on a side and 1 – 2 mm thick. Platinum and silver paste electrodes were used, and some samples were tested using gold wire for connection to the measurement leads. Painted samples were initially fired in air to adhere the electrodes, but the atmosphere was later switched to dry 9 % H_2/N_2 to maintain the reduced state of the samples, thereby shortening the time needed to reach equilibrium during testing.

Schematics of the various conductivity rigs used to test pure STN95, pure BCZY27, and composite samples are shown in Fig. 1. The 4-point probe DC method (Fig. 1a) was used to collect the resistance data over time for STN95 bar samples. DC conductivity measurements for the BCZY27 pellet samples were taken using the pseudo 4-point method, whereby the working and sense wires were connected to the same current collector electrode (platinum mesh), and the counter and sense wires were connected to the opposite electrode (Fig. 1b). A Keithley model 580 micro-ohmmeter was used for the 4-point probe measurements. The pseudo-4-point DC measurements were carried out with a Keithley model 2700 multimeter, as well as with a Gamry Reference 600® Potentiostat/Galvanostat in single-point galvanostatic mode. Samples tested with the Gamry were suspended from the Pt working and sense wires by Au wires connected to Ag mesh current collectors adhered to Ag paste electrodes on each side of the sample (Fig. 1c).

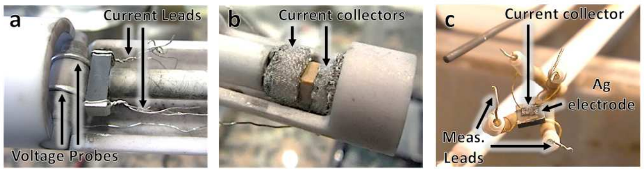

Fig. 1 Images of conductivity measurement rigs: **a** STN95 bar in a 4-point DC configuration, **b** BS27_5050 sample in pseudo 4-point DC configuration (Keithley connection), and **c** BS27_4060 sample in pseudo 4-point DC configuration (Gamry connection). The light color of the BS27 sample edges in **b** is due to surface oxidation during electrode firing in air.

The rigs shown in Fig. 1 were inserted in sealed tube furnaces equipped with programmable temperature control and gas supply systems. All testing was done under a gas environment chosen to approximate hydrogen separation conditions, i.e., a humidified, diluted hydrogen atmosphere, typically 6 – 9 % H_2 balanced with an inert gas (N_2, Ar, or He). Refrigerated and room-temperature bubblers were used to supply moisture to the gas stream between 1 – 3 % vol. H_2O.

STN95 conductivity vs. synthesis route

During the study, samples of STN95 were also produced by SPS to make a more accurate comparison as an end-member composition versus the BS27 composite samples. The same SPS profile was used to create STN95 samples as was used for BS27 samples.[12] These SPS-made STN95 samples were fabricated as disc-shaped pellets of 15 mm ∅ and 1 – 2 mm thickness. Platinum electrodes were painted onto the samples and were fired at 1100 °C for 2 h in 5 % H_2/Ar. Silver mesh current collectors and gold wire leads were then attached with silver paste, following the same preparation procedures as in the previous section. The rig configuration from Fig. 1c was used to connect the STN95-SPS samples to the same Gamry instrument used for the BS27 samples.

Hydrogen flux measurements

BS27 flux samples were ground flat to 1 mm thickness before testing. Hydrogen flux was measured in pure permeation mode by gas chromatography. Two types of test stands and sealing methods were used in the measurements: 1) a horizontal configuration with a gold foil ring seal, held in place by a spring loaded alumina ring on the feed side of the sample, and 2) a vertical configuration with glass as the seal, covered by a short alumina tube ground to sit like a cap on top of the sample. Schematics of both rigs are given in Fig. 2.

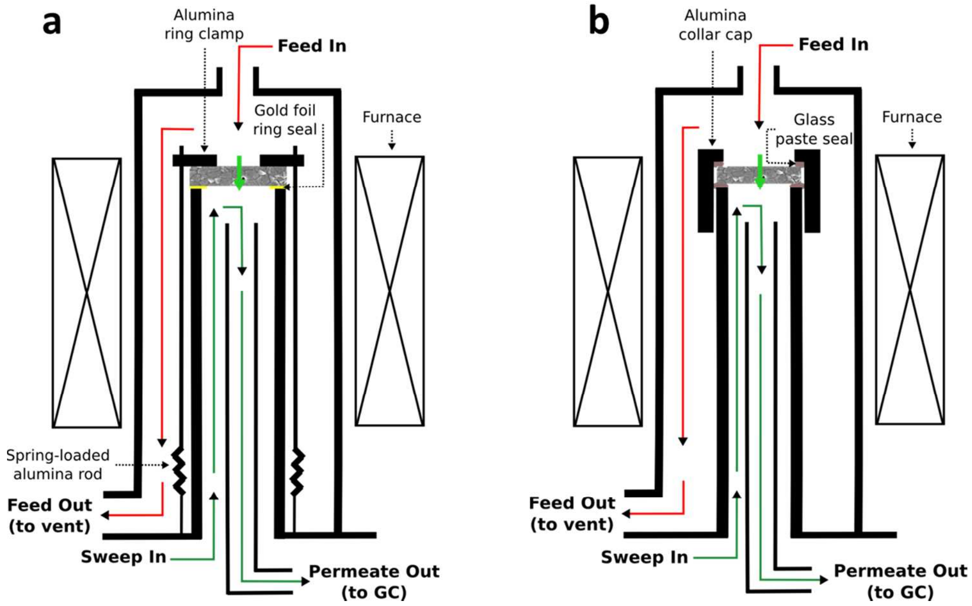

Fig. 2 Schematic diagrams of hydrogen permeation test rigs shown in cross-section: **a** rig 1, a horizontal configuration involving a gold foil ring seal and spring-loaded ceramic clamp ring, and **b** rig 2, a vertical configuration with a glass seal and ceramic collar cap. Both schematics are displayed in a vertical format for easier viewing. GC refers to gas chromatograph.

A gas chromatograph (CP-4900 MicroGC, Agilent) with Ar carrier gas was connected to the outlet of the permeate (sweep) side. Dry Ar, as well as dry 100 ppm H_2/Ar, were used as sweep gases to test the effect of a finite $p(H_2)$ gradient on membrane performance. A feed gas of dry and moist (3 % H_2O) 9 % H_2 balanced with He was used. The flow rates of the feed and sweep gases were kept equivalent during testing.

Creating a gas-tight seal between the feed and permeate sides proved difficult. Several methods were used, including Thermiculite®, which did not perform correctly, and gold foil rings and glass powder, both of which sufficed for the purposes of the work. For the samples tested in the horizontal configuration (*cf.* Fig. 2a) gold foil rings (0.2 mm thick) were pressed between the sample and the permeate alumina tube supporting it. A thick alumina ring connected to the rig's base by spring-loaded alumina rods held the sample and gold ring tight against the permeate tube, simultaneously creating a well-defined exposed area of the sample on the feed side. The gold seal was heat-treated at 1030 °C for 12 h in 9 % H_2/N_2, after which the rig was cooled to the first testing temperature at 90 $°C{\cdot}h^{-1}$ to minimize thermal stresses.

Samples tested in vertical configuration (*cf.* Fig. 2b) were sealed with a glass powder ($CaO\text{-}BaO\text{-}SiO_2$, GA-13, Nippon Electric Glass, Ltd.) mixed with α-terpineol to form a paste that was applied between the alumina permeate tube and sample, and between the alumina collar cap and the feed side of the sample. The glass seal was heated to 900 °C for 1 h in the testing atmosphere (9 % H_2/He), and then cooled to the testing temperatures. A heating rate of 90 $°C{\cdot}h^{-1}$ was used up to 600 °C, after which heating was slowed to 60 $°C{\cdot}h^{-1}$ to minimalize thermal stress. After the 1 h hold at 900 °C, the system was cooled to 800 °C at 45 $°C{\cdot}h^{-1}$. This rate was also used to cool and heat between 600 and 800 °C during flux testing.

At the testing temperatures, leaks of 1 – 3 $mL{\cdot}min^{-1}$ were observed for flux tests performed in rig 1. A leak of 0.32 $mL{\cdot}min^{-1}$ was achieved in consecutive tests with the glass seal method in rig 2, representing the best results for all flux testing in the current work. During a third test in rig 2, a larger leak of 0.8 $mL{\cdot}min^{-1}$ was observed, and was attributed to insufficient application of glass to the seal zone. Binary gas mixture theory was used to correct the measured flux for the leaks. Effective diffusion coefficients for H_2 and He in Ar were calculated, and a ratio of these coefficients was applied as a correction factor for the H_2 signal observed by the GC. By this method, approximately 10 % more H_2 than the feed ratio (9 % H_2/He) was calculated to pass through the leak. The calculations were performed for each testing temperature, but the correction factors varied by less than 0.5 %, so the ratio of H_2 to He in the leak was assumed to be constant during the tests. Details of the GC calibration procedure, an example of raw data, and the leak correction method are given in the Supplementary Materials.[†]

Effect of sweep atmosphere on STN95

A sintered sample of STN95 (150 mg) was tested for oxidation under flux sweep conditions by thermogravimetric analysis (TGA). The thermogravimetric analyzer utilizes a microbalance (Thermo Cahn D-200) capable of measuring a 150 mg weight change with a resolution of 0.1 µg. The sample was placed in an alumina crucible that hung from a nichrome wire attached to the microbalance. Gas mixtures were supplied via three mass flow controllers (Alicat Scientific MC series), each with a maximum volumetric flow rate of 50 $mL{\cdot}min^{-1}$ (sccm). The sample was initially exposed to moist 3.5 % H_2/N_2 during heating to 700 °C (200 $°C{\cdot}h^{-1}$), humidified by a room-temperature bubbler. Once equilibrium was reached at 700 °C, the gas was changed to moist argon. These TGA experiments were conducted to determine the extent to which the $p(O_2)$ in the sweep would alter the conductivity of STN95 during hydrogen flux measurements when only dry argon was used as the sweep gas, assuming known defect mechanisms and their dependence on $p(O_2)$.

Microstructure vs. composition

As previously observed in high-resolution transmission electron microscopy analysis of BS27_5050 samples,[12] the microstructures of SPS-fabricated samples were inhomogeneous. A wide range of grain sizes from ~30 nm – 1 µm were observed and no obvious spatial patterns were seen in the analysis. Further comparisons of composite microstructure across the compositional range were collected using a scanning electron microscope equipped with a focused-ion beam (FIB-SEM, Helios NanoLab 600i, FEI). A through-lens detector (TLD) in both secondary (SE) and backscattered electron (BSE) modes was used to collect images. Cross-sectional areas of 50 µm^2 (10 x 5 µm) were made at multiple locations across each sample, both in SE and BSE detector modes.

Composite conductivity modeling

To describe the effective conductivity behavior of a composite material, a variety of composite conductivity models have been proposed in the literature.[13-15] The effective medium treatment by Bruggeman,[13] later expanded by Landauer[14] and others,[16,17] serves as a common foundation for many approaches. The symmetric Bruggeman-Landauer effective medium model (BL) is one of the more widely-used descriptions for conduction in two-phase composites, and can be expressed as:

$$x_1 \frac{\sigma_m - \sigma_1}{2\sigma_m + \sigma_1} + x_2 \frac{\sigma_m - \sigma_2}{2\sigma_m + \sigma_2} = 0\,, \tag{1}$$

where σ_1 and σ_2 are the conductivities of phases 1 and 2, x_1 and x_2 are the volume fractions of phases 1 and 2, and σ_m is the effective conductivity of the composite. STN95 is given to be phase 1 and BCZY27 to be phase 2. It is assumed that $x_1 + x_2 = 1$. This model is known as the symmetric BL model and it is best applied under the assumption that neither phase in the composite is blocked or restricted by the other.[18] This model shows a rudimentary form of percolation, with a threshold of about 0.33.

A more recent model developed by Wu and Liu (WL)[15] builds on Equation (1) for two mixed-conducting phases in a composite. For the limiting case where one phase is completely electronic and the other completely ionic, the model assumes that the boundaries between the two phases exhibit infinite impedance. This assumption results in the following piecewise expression for σ_m:

$$\sigma_m = \begin{cases} \left(1 - \frac{3}{2}x_1\right)\sigma_2 & \text{if } x_1 \le \frac{1}{3} \\ \left(1 - \frac{3}{2}x_1\right)\sigma_2 + \left(\frac{3}{2}x_1 - \frac{1}{2}\right)\sigma_1 & \text{if } \frac{1}{3} \le x_1 \le \frac{2}{3}\,, \\ \left(\frac{3}{2}x_1 - \frac{1}{2}\right)\sigma_2 & \text{if } x_1 \ge \frac{2}{3} \end{cases} \tag{2}$$

where again, $x_1 + x_2 = 1$. Equation (2) is akin to solving Eq. (1) twice, once for $\sigma_1 = 0$, once for $\sigma_2 = 0$, and then summing the results. The BL and WL models provide reasonable upper and lower bounds, respectively, for an initial assessment of the experimental conductivity data gathered for BS27.

Results

DC Conductivity of STN95, BCZY27 and BS27

Fig. 3 displays a summary of total conductivity gathered in moist (1 – 3 % H_2O) 9 % H_2/(N_2, He, Ar) for pure STN95, pure BCZY27, and composite samples of BS27_5050, BS27_4060, and BS27_3070 as a function of inverse temperature.

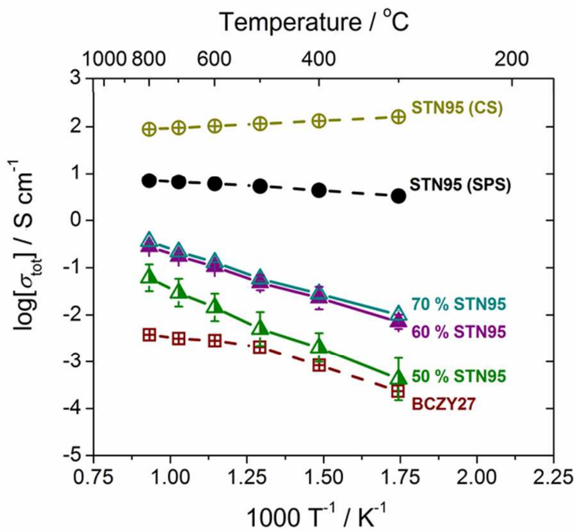

Fig. 3 Total conductivity data taken in wet (1 – 3 % H_2O) 9 % H_2/(N_2, He, Ar) for pure STN95 (by conventional sintering (CS) and spark plasma sintering (SPS) routes), for pure BCZY27 (CS), and for BS27 composite samples of three compositions, labeled by the volume percentage of STN95. Several samples of each BS27 composition were tested. Error bars show the standard deviation in the BS27 data.

For the composite samples, the scatter in the conductivity data decreased with increasing STN95 content. Comparing composite samples of like composition, the inhomogeneous microstructures and variable grain size distributions generated by the SPS process appear to have minimal impact on total conductivity. Microstructural investigations by electron microscopy partly revealed the nature of STN95–BCZY27 phase interaction, and contributed to an improved electrical properties model for the composite (see Discussion).

STN95 conductivity vs. synthesis route

The contrast in total conductivity magnitude and temperature dependence between CS and SPS-produced STN95 samples indicates that the STN microstructure has a significant impact on its electrical properties and, hence, those of the composite. Grain sizes for STN95-CS samples were on the order of several microns with a qualitatively narrow distribution, whereas STN95-SPS samples exhibited smaller grains ranging from 50 – 500 nm, having a broader distribution. STN95-CS samples showed total conductivities on the order of 100 S·cm^{-1}, while the same composition prepared by SPS yielded an order of magnitude lower conductivity (~10 S·cm^{-1}). Additionally, STN95-SPS samples showed a weak semiconductor-like activated temperature dependence, in contrast to the metallic character observed for the STN95-CS samples.

Hydrogen permeation

Hydrogen flux experiments were done under non-galvanic conditions without catalysts to investigate the inherent hydrogen permeability of BS27 as a function of BCZY27 content. When only dry argon was used as the sweep gas, hydrogen flux was measurable over a persistent leak, with a maximum value of 0.007 µmol·cm^{-2}·s^{-1} at 800 °C for BS27_5050. No measureable flux was observed for BS27_4060 or BS27_3070 samples. Furthermore, the addition of water vapor to the feed gas composition had no impact on the hydrogen flux for any BS27 composition under any test condition, suggesting that the oxide ion conductivity component was negligible in these systems.

Since the conductivity data in Fig. 3 hint at high interfacial impedance between the two phases in the composite material, it was hypothesized that the protons and electrons could not easily recombine when they reached the permeate side. That is, the following reaction might be limited at the sample surfaces:

$$2OH_O^{\bullet} + 2e' \rightarrow H_2(g) + 2O_O^{x} \tag{3}$$

To test this hypothesis, a sample of BS27_5050 (90 % dense) was prepared with palladium catalyst layers deposited by room-temperature sputtering on both sides. The Pd layers facilitate the dissociation and recombination of protons and electrons at the feed and permeate sides of the membrane, respectively. The thickness of the layers was estimated to be 100 nm, based on calibration of the sputtering equipment by profilometry. A scanning electron micrograph (in backscattered mode) of the sample surface, showing the Pd layer is provided in Fig. 4. The sample holder clip in the sputtering chamber blocked a portion of the sample from being coated, which provided contrast between the sputtered and plain surfaces (*cf.* inset of Fig. 4). The bare portion of the sample was outside the active area during permeation testing.

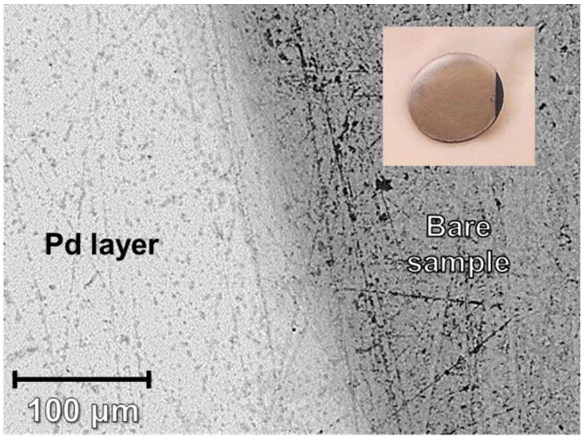

Fig. 4 Backscattered electron micrograph taken of a BS27_5050 sample surface before flux testing, centered on the sputtered Pd layer boundary. A photograph of the sample is inset at top right.

The hydrogen permeation of the Pd-coated BS27_5050 sample was tested in rig configuration 2 (*cf.* Fig. 2b). The measured flux was corrected for a 0.8 mL·min^{-1} leak. The results were compared to the test on a plain BS27_5050 sample where a 0.32 mL·min^{-1} leak was observed, and are presented in Fig. 5.

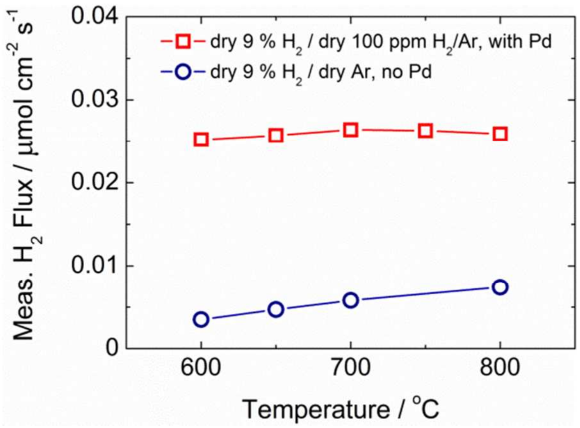

Fig. 5 Leak-corrected hydrogen permeation values for a BS27_5050 sample with Pd layers (squares) and a plain BS27_5050 sample (circles). The feed and permeate gas conditions are given in the figure legend.

The presence of the Pd catalyst layers boosted the measured hydrogen flux by 4 – 7 times, a modest improvement. Adding 100 ppm of H_2 to the sweep did not appear to have an impact, since all tests in the current work were hampered by leaks from the feed to permeate sides, i.e., the hydrogen chemical potential gradient was effectively set by the leak.

Effect of sweep composition on STN95

In conductivity testing on STN95-CS, a decrease in the total conductivity of 100× was observed when switching from dry dilute H_2/N_2 to dry Ar. TGA experiments conducted on a STN95-CS sample showed a weight increase of 0.05 % (~75 µg) after ~14 h in moist Ar. This increase amounts to ~5 µmol of atomic oxygen. Since the electronic conductivity in STN is due to reduced titanium ions, i.e., Ti^{3+}/Ti^{4+} redox couples, equal in concentration to the substitution ion Nb^{5+},[19] the oxidation of the reduced ions by the incorporated oxygen is calculated to be 11 % of the Ti^{3+} concentration. A plot of the TGA data is given in the Supplementary Materials.[†] STN95-CS shows metallic-type conductivity behavior with increasing temperature, but when $p(O_2)$ increases to moderate values (> 10^{-8} atm) at high temperature, Sr vacancies begin to dominate the defect chemistry, consequently lowering the *n*-type conductivity substantially.[19]

Microstructural investigation

Several samples of each BS27 composition were analyzed with FIB-SEM to investigate the grain size and interfacial boundary volume between BCZY27 and STN95. A selection of FIB section micrographs (SE) and magnified microstructures (BSE) for all three compositions is given in Fig. 6. The darker phase corresponds to STN95 and the lighter phase corresponds to BCZY27.

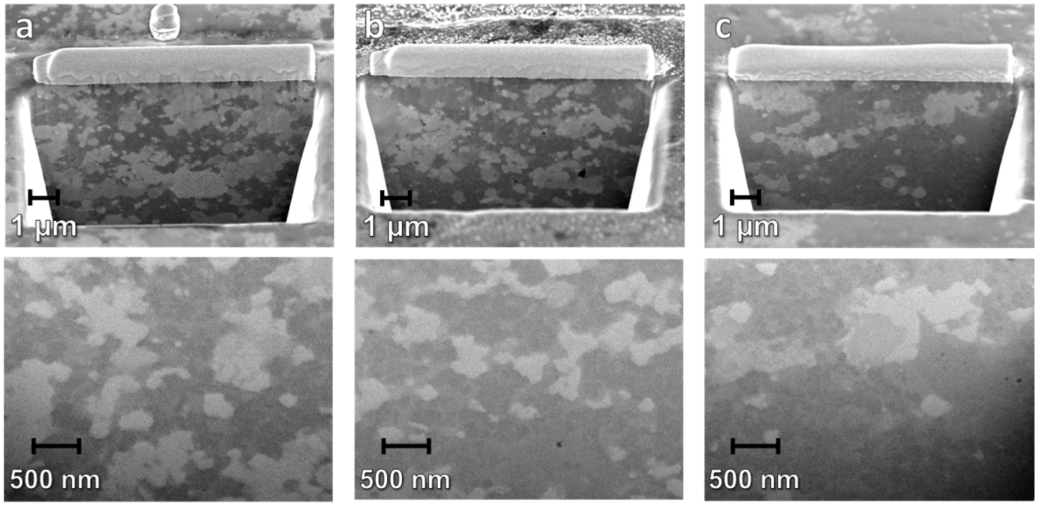

Fig. 6 Scanning electron micrographs of FIB cross-sections for **a** BS27_5050, **b** BS27_4060, and **c** BS27_3070 samples. The images in the top row were taken in secondary electron mode while those in the bottom row were taken at higher magnification in backscattered mode. The darker phase corresponds to STN95 and the lighter phase to BCZY27.

The grain size in BS27 SPS samples varied widely, from 30 nm to 1 µm, with the majority of grains below 500 nm. Several cross-sections were made on each sample, and there appeared to be no spatial patterns in the grain size or phase distribution, which corroborates previous observations by scanning transmission electron microscopy on a BS27_5050 sample.[12] The percolation of both phases is best exemplified in BS27_5050, whereas the BCZY27 phase appears more isolated in the 60 and 70 volume % STN95 samples. Estimates of contact area length between STN95 and BCZY27 were performed using *ImageJ* software for the purposes of validating the conductivity modeling effort (*cf*. Table 2).

Discussion

Conductivity modeling

As shown in Fig. 3, the conductivities of the composite samples are low compared to the STN95 values, and appear to be limited by the conductivity of the BCZY27 phase. The STN95 phase in the BS27 SPS-produced composites is likely best represented by the STN95-SPS samples, but even so this only partially explains the overall low conductivity of BS27 composites. Standard effective medium models, such as the Bruggeman-Landauer (BL) and Wu-Liu (WL) models do not accurately predict the experimental data, presumably because they do not account for interfacial effects between the phases or at boundaries of the same phase.

Under hydrogen flux conditions, the BL and WL models seem intuitively appropriate for a composite like BS27, as there are no reports of significant *n*-type conductivity in BCZY27, nor of any significant protonic conductivity in STN95. However, the disparity between the BS27 data and the models underlines the need for a new effective medium model that includes the option to incorporate a finite, non-zero interfacial conductivity between the two phases, σ_c, in an attempt to better explain the experimental data. Using Eq. (1) as a foundation, an expression that satisfies this condition was recently developed in the context of a composite consisting of two different ionic conductors:[20]

$$\left(\frac{\sigma_m-\sigma_1}{2\sigma_m+\sigma_1}\right){x_1}^2+\left(\frac{\sigma_m-\sigma_2}{2\sigma_m+\sigma_2}\right){x_2}^2+\left(\frac{\sigma_m-\frac{1}{\frac{1}{\sigma_1}+\frac{1}{2\sigma_c}}}{2\sigma_m+\frac{1}{\frac{1}{\sigma_1}+\frac{1}{2\sigma_c}}}+\frac{\sigma_m-\frac{1}{\frac{1}{\sigma_2}+\frac{1}{2\sigma_c}}}{2\sigma_m+\frac{1}{\frac{1}{\sigma_2}+\frac{1}{2\sigma_c}}}\right)x_1x_2=0 \qquad (4)$$

where again, x_1 and x_2 are the volume fractions of STN95 and BCZY27, respectively, and σ_1 and σ_2 are the conductivities of STN95 and BCZY27, respectively. This formula is dubbed the interfacial effective medium (IEM) model. In Equation (4), the conductivities σ have the usual units of S·cm^{-1}. Note that this definition also holds for σ_c, which is defined here as:

$$\sigma_c=\frac{G_{AS}}{A'}\,, \qquad (5)$$

where G_{AS} (units of S·cm^{-2}) is the interfacial area-specific conductance, i.e., the inverse of the contact area-specific resistance (ASR$_c$), and *A'* is the amount of contact length between STN95 and BCZY27 phases per unit area of composite (units of cm·cm^{-2}, or cm^{-1}). Several factors can be linked to the physical origin of a finite G_{AS}, including structural or chemical inhomogeneities at the heterojunctions, interfacial phase-segregation, or space charge effects. Experimental data can be fitted with this model to extract values of σ_c, which can then be physically interpreted with the more meaningful terms G_{AS} and *A'*. For experimental validation of this model, *A'* can be determined in a relatively straightforward manner through estimations of contact boundary length from electron micrographs. However, determining G_{AS} experimentally requires careful impedance analysis of a geometrically well-defined interface, *e.g.*, via a cone electrode experiment, as has been done for STN/YSZ junctions,[21] or a thin-film model-electrode. Experimental confirmation of G_{AS} was not, however, achieved in the current work.

In Fig. 7, Eq. (4) is plotted as a function of STN95 content at 700 °C, for a range of σ_c values from zero to 10 S·cm^{-1} (solid curves), together with the Bruggeman-Landauer (BL) model (long dash curve) and Wu-Liu (WL) model (short dash curve), and overlaid with the BS27 experimental data (*cf.* Fig. 3). The IEM curves in Fig. 7 were generated using the STN95-SPS data as the end-member composition. Error bars for the experimental data represent the standard deviation in the measured total conductivity.

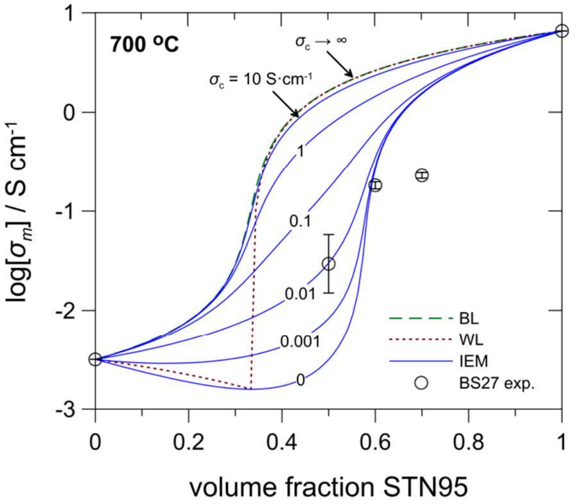

Fig. 7 Total conductivity of the BS27 composite (σ_m) at 700 °C as a function of STN95 volume fraction (x_1), compared to the BL and WL models, and with the IEM model (Eq. (4), solved for $\sigma_c = 0 – 10$ S·cm^{-1}). The BL curve (long dash) overlays with the IEM model (σ_c = 10) up to $x_1 = 0.33$, whereupon it tracks with the WL curve (short dash), and is equivalent to solving the IEM model for $\sigma_c \rightarrow \infty$. The end-member points correspond to the pure BCZY27-CS and STN95-SPS values (*cf.* Fig. 3). The error bars on the BS27 points represent the standard deviation in the experimental data.

The IEM model of Eq. (4) provides a more accurate description of BS27 conductivity, but still does not fully describe the electrical properties of the composite. Given the broad grain size distributions observed in the samples, coupled with the inhomogeneity of the microstructures, the electrical properties of BS27 are non-trivial to simulate. Furthermore, given the dissimilar charge transfer properties of STN95 and BCZY27, the formation of a space charge layer (SCL) at the contacts between the phases cannot be overlooked. SCL theory has been used to describe the electrical properties of junctions or contacts in many materials and devices, particularly in semiconductors[22] and in electrolytes or solid-state ionic conductors.[23-27] Depending on the type of charge carriers that contribute to the partial currents in a material, SCL can enhance (accumulation scenario) or inhibit (depletion scenario) charge transport in the vicinity of a junction. A definition for the SCL width (δ), adapted from semiconductor theory,[28] is presented in Equation (6) in relation to the material properties of STN95 and BCZY27:

$$\delta = \sqrt{\frac{2V_0\varepsilon_0}{q}\left(\frac{\varepsilon_{\mathrm{H}^+}}{N_{\mathrm{H}^+}} + \frac{\varepsilon_{\mathrm{e}^-}}{N_{\mathrm{e}^-}}\right)}, \tag{6}$$

where V_0 is the built-in voltage between STN95 and BCZY27 junctions, defined by the difference in work functions, q is the fundamental charge, ε_0 is permittivity of free space, ε_{H+} is the dielectric constant of BCZY27, ε_{e-} is the dielectric constant of STN95, N_{H+} is the estimated protonic carrier concentration in BCZY27, and N_{e-} is the estimated *n*-type electronic carrier concentration in STN95. Values for these quantities, summarized in Table 1, were obtained from the available literature, and from best-guess estimates when supporting information was not found.

Table 1 Values of relative dielectric constant, electronic or protonic carrier concentration, and work function for STN95 and BCZY27. Literature-based values are in regular font, while best-guess values are in italics.

Material	ε (relative)	N (cm^{-3})	Φ (eV)
STN95	*300*	1.8 x 10^{21}	*4*
BCZY27	36	2.9 x 10^{20}	*6*

An approximation for the dielectric constant of BCZY27 was made based on unpublished work. The work function of BCZY27 has not been reported in the literature, but, since the material is an acceptor-doped semiconductor-type oxide, Φ is suspected to be moderately large, and was set to 6 eV for the current work. Assuming a 30 % protonated BCZY27 phase,[9] N_{H+} was determined to be 2.9 x 10^{20} cm^{-3}, based on lattice volume calculations.

Microwave dielectric research on $SrTi_{1-x}Nb_xO_3$ (x < 0.01) materials and donor-doped $Sr_{1-x}La_xTiO_3$[29,30] was referenced to estimate ε and Φ for STN95. The dielectric constant of a material similar to STN95, $Sr_{0.94}Ti_{0.9}Nb_{0.1}O_{3-\delta}$ (STN94), has been measured to be ~300 at low and ambient temperatures (-18 – +60 °C), but is not known at higher temperatures, i.e., under the conductivity or hydrogen flux test conditions used in this study. Abrantes et al.[31] studied the dielectric properties of undoped $SrTiO_3$ up to 600 °C and reported a value of ~900 for ε in N_2. The carrier concentration of conduction-band electrons in STN95 was taken from the work of Blennow et al.,[19] confirming an earlier study by Tomio et al.[32] The applicability of the dielectric and work function experiments to STN95 is uncertain at best, given the different electrical properties between undoped and Nb-doped $SrTiO_3$, doping amounts and charge compensation mechanisms, as well as differences in processing routes. To accurately investigate the dielectric properties of STN95 under testing conditions, a network analyzer, which could measure the impedance at gigahertz frequencies, would be required, and such equipment was not available for the current work. Since the conductivity of STN95-SPS is of the order of 10 S·cm^{-1} at 700 °C, a lower value of ε was assumed, in line with the low-temperature measurements on STN94.

An approximate SCL width of 6 nm was calculated from the values in Table 1, utilizing Eq. (6). Within the SCL, the carrier concentrations of protons (BCZY27) and electrons (STN95) were assumed to decrease exponentially with distance toward the heterojunction, away from the bulk of the respective phase, according to a Boltzmann approximation.[33] Thus, the spatial variation of conductivity with distance across the SCL, $\sigma(x)$, can be approximated as

$$\sigma(x) = \sigma_{\mathrm{STN95}}\, e^{-\frac{\left(w_{\mathrm{e}^-}+x\right)}{\delta}} + \sigma_{\mathrm{BCZY27}}\, e^{-\frac{\left(w_{\mathrm{H}^+}-x\right)}{\delta}}, \tag{7}$$

where w_{e-} and w_{H+} are the so-called depletion widths on each side of the heterojunction, summing to the total SCL width, and set to $\delta/2$ for these calculations. Inverting Eq. (7) and integrating over the total depletion width enables the calculation of an effective area-specific resistance (ASR_c) for the interfacial contact region by Equation (8):

$$\mathrm{ASR}_{\mathrm{c}} = \int_{-w_{\mathrm{e}^-}}^{+w_{\mathrm{H}^+}} \frac{1}{\sigma(x)}\,dx\,. \tag{8}$$

Setting Eq. (8) equal to $(G_{AS})^{-1}$ from Eq. (5) links the interfacial conductance directly to the properties of the SCL.

With the SCL thickness calculated from Eq. (6), an interfacial conductance (G_{AS}) of 6.1 x 10^4 S·cm^{-2} was obtained, which, combined with the estimated interfacial length per area of contact between STN95 and BCZY27, A' (cm^{-1}), was inserted back into Eq. (5) to calculate σ_c, as a check for the IEM model. Values for A' and calculated σ_c are given in Table 2 for each BS27 composition.

Table 2: Estimated interfacial length/area values (cm^{-1}) between STN95 and BCZY27 in BS27 composites using *ImageJ* software and the corresponding calculated σ_c values (Eq. (5)).

Composition	A' (cm^{-1})	σ_c (S·cm^{-1})
BS27_5050	3.3 x 10^4	0.018
BS27_4060	2.7 x 10^4	0.022
BS27_3070	2.3 x 10^4	0.026

The values for calculated σ_c are in agreement with the best fit curve from the IEM model for the experimental data (0.01 S·cm^{-1}).

In addition to the contact resistance between the two phases in the composite, we also speculate that resistive layers may form at STN95 homojunctions during SPS, or during conductivity testing, which would bring down the overall conductivity, thus explaining the remaining overprediction of the IEM model at high STN95 content. This suggested homojunction effect would likely occur in parallel with space charge effects at the heterojunctions, and would dominate at higher STN95 contents as the number of homojunctions increase while the number of heterojunctions decreases. Additionally, charge transfer between the phases may be occurring, and could be attributed to electronic conductivity in the BCZY27 phase promoted by reduction of Ce^{4+} to Ce^{3+} during testing.

The most important conclusion from this study is that the conductivity of BS27, even at 70 volume % STN95, shows temperature-activated behavior similar to the BCZY27 phase, and is restrained to an overall low value, discouraging efforts to optimize its performance as a hydrogen separation membrane, especially in pressure-driven (non-galvanic) configurations.

Hydrogen permeation

The measured hydrogen flux recorded for BS27_5050 indicates moderate performance for a composite cercer material. This performance can be examined in the context of a common model for hydrogen flux in an ambipolar mixed electron-proton conducting membrane where protons are the majority defect:

$$j_{H^+} = \frac{-RT\sigma_{H^+}\varphi_{H^+}}{2F^2L\alpha}\left(\ln[p_{H_2II}]-\ln[p_{H_2I}]\right), \tag{9}$$

where R is the universal gas constant (J·mol^{-1}·K^{-1}), T is the test temperature (K), σ_{H+} is the protonic conductivity (S·cm^{-1}), F is Faraday's constant (C·mol^{-1}), L is the membrane thickness (cm), and p_{H2} is the dimensionless partial pressure of hydrogen. The expression has been modified from a related work[34] to include the terms φ_{H+}, the volume fraction of the proton-conducting BCZY27 phase, and α, a factor indicating the tortuosity of the BCZY27 phase in the composite. The incorporation of α into flux calculations was recently proposed by Ricote et al. for a two-phase cercer mixed electron-proton conducting composite.[35]

Eq. (9) is valid for the following conditions: 1) the electronic conductivity is high enough to make the transference number t_{e-} unity, 2) protons are the majority defect, and 3) acceptor-dopant ions are the compensating mechanism for the protons. For BS27_5050 $\varphi_{H+} = 0.5$, and for this work, α was set to 1.5, based on theoretical treatments of composite fuel cell materials available in the literature.[18,36,37] Eq. (9) is integrated over a known hydrogen chemical potential gradient, the driving force for hydrogen flux, from $p_{H2,I}$ (high) to $p_{H2,II}$ (low), hence the need for the negative sign at the front to generate a positive value. For a protonic conductivity of 2.8 mS·cm^{-1} (corresponding to the value measured for BCZY27 at 600 °C in Fig. 3) and setting $p_{H2,II}$ to the value of the leak, Eq. (9) produces a value of 0.0172 µmol·cm^{-2}·s^{-1}, roughly five times greater than the measured value of 0.0035 µmol·cm^{-2}·s^{-1} for BS27_5050 at 600 °C when dry argon was used as the sweep. It should be noted that increasing α to 7 (all else the same) produces a predicted flux of 0.0036 µmol·cm^{-2}·s^{-1}, suggesting a strong dependence on microstructure.

Comparing the results of plain BS27_5050 (no Pd layers) to other hydrogen separation membrane research, a recent study on Ca-doped $LaNbO_4/LaNb_3O_9$ composite cercer membranes prepared by SPS reported hydrogen flux values an order of magnitude lower than BS27_5050 under the same test conditions.[38] The permeative flux for BS27_5050 is comparable to values reported for single-phase membranes such as Y-doped $SrCeO_3$,[39] Eu-doped $SrCeO_3$,[40,41] and Mo-substituted lanthanum tungstate ($La_{27}Mo_{1.5}W_{3.5}O_{55.5}$).[42] However, the performance does not match that of ceramic-metal (cermet) composites such as Ni-$BaZr_{0.1}Ce_{0.7}Y_{0.1}Yb_{0.1}O_{3-\delta}$[43] and Ni-$BaZr_{0.1}Ce_{0.7}Y_{0.2}O_{3-\delta}$,[44] as well as of another recently-studied cercer, $La_{5.5}WO_{11.25-\delta}$ /$La_{0.87}Sr_{0.13}CrO_{3-\delta}$ (LWO-LSC).[45] The application of Pd layers to a BS27_5050 sample improved the hydrogen flux performance by a factor of 4 – 7 across the temperature range investigated. Yet, even the best performance at 700 °C still falls roughly an order of magnitude short of the 1 mL·cm^{-2}·min^{-1} (0.74 µmol·cm^{-2}·s^{-1}) benchmark desired for commercial applications.[1]

The TGA experiments suggest STN95 does not significantly oxidize in the presence of a moist Ar atmosphere at high temperature. Based on the calculation of incorporated oxygen from the 0.05 % weight gain, and assuming a classical relationship between carrier concentration and conductivity, 11 % of Ti^{3+} ions becoming oxidized cannot account for the precipitous drop in total conductivity. Rather, it is likely that the reduction in *n*-type conductivity is caused by Sr-vacancies becoming a majority defect compensation mechanism in moderately oxidizing environments, which has been reported in the literature.[19,32,46] The presence of H_2 in the sweep, whether by leak or intentional addition, maintained the conductivity of STN95 in the 10^2 S·cm^{-1} range, which seems to have a beneficial impact on the permeation performance, and indicates that maintaining a reducing environment on both sides of the BS27 membrane is crucial. Since leak-free testing was not achieved, the effect of adding small partial pressures of H_2 to the sweep could not be determined.

Based on the microstructural investigations of the three BS27 compositions, it appears the BCZY27 phase is isolated and non-percolating in the 60 and 70 volume % STN95 samples, hence the lack of measured hydrogen flux for these compositions. The isolation of the BCZY27 phase is thought to be due to insufficient mixing of the powders during synthesis. The phenomenon may also be attributed to the non-homogenous sintering conditions inherent to SPS, e.g., radial temperature gradients in the sample causing the STN95 and BCZY27 phases to sinter differently. The end result is that the protonic transport pathways are severely limited in BS27_4060 and BS27_3070 samples, effectively eliminating any hydrogen flux potential. While increasing STN95 content improved total conductivity by 5 – 10× at permeation testing temperatures, the hydrogen permeability was nullified, indicating the BCZY27 phase is rate-limiting for this membrane material.

Conclusions

The conductivity and hydrogen permeability of BCZY27/STN95 (BS27) composite cercer compositions of 50, 60, and 70 volume % STN95 were measured. The total conductivity for BS27 is significantly lower than the prediction given by standard effective medium theories for composite electrical properties. Thus, a modified effective medium model explicitly accounting for interfacial effects between the two phases was developed. This interfacial effective medium (IEM) model more accurately described the response of BS27, but does not fully describe the electrical properties at high STN95 volume fractions (>60 %). Calculations of interfacial conductivities based on space charge layer theory are consistent with the value of the interfacial resistance obtained from the IEM calculations. Hydrogen flux was observed only for BS27_5050 samples, indicating that boosting the total conductivity by adding more STN95 chokes off the proton-conducting BCZY27 phase. The performance of BS27_5050 in pure permeation mode (without catalysts or electrodes) was 0.004 – 0.008 $\mu mol \cdot cm^{-2} \cdot s^{-1}$ from 600 – 800 °C, and is comparable to some single-phase and cercer ceramic membrane materials, while falling short of many cermets and at least one new cercer membrane. The deposition of thin palladium layers (100 nm) to a BS27_5050 sample by sputtering improved the measured flux at 700 °C by a factor of 4.5 to a maximum of 0.026 $\mu mol \cdot cm^{-2} \cdot s^{-1}$. Overall, there are a number of challenges to optimizing BS27 as a competitive hydrogen separation material.

Acknowledgements

The work was supported in part by internal funds from the Technical University of Denmark (DTU) under the Proton Conducting Fuel Cells (PCFC) project, and by the Renewable Energy Materials Research Science and Engineering Center at the Colorado School of Mines under National Science Foundation grant no. DMR-0820518. The authors gratefully recognize the input of Prof. Peter Vang Hendriksen (DTU) for valuable discussions and guidance on correcting the hydrogen flux data for leaks. Thanks are also due to Dr. Davide Ippolito (DTU) for help setting up and executing some of the GC experiments, to Prof. Colin Wolden and Daniel Cooney (CSM) for sputtering the palladium layers on the BS27_5050 flux sample, and to Dr. Michael Sanders (CSM) for valuable discussions on experimentation and modeling. Finally, Dr. Li Han is thanked for providing the crucial STN95-SPS sample.

Notes and references

[a] Department of Energy Conversion and Storage, Technical University of Denmark, Risø Campus, Frederiksborgvej 399, 4000 Roskilde, Denmark
[b] Renewable Energy Materials Research Science and Engineering Center, Department of Metallurgical and Materials Engineering, Colorado School of Mines, 1500 Illinois St., Golden, CO, 80401, USA
[c] Mechanical Engineering Department, Colorado Fuel Cell Center, 1310 Maple St., Golden, CO 80401, USA

† Electronic Supplementary Information (ESI) available: hydrogen flux measurement leak correction method. See DOI: 10.1039/b000000x/

1 W. G. Coors, *One Million Liter per Day Gas-to-Liquid Refinery*, Report Proton-CT30, CoorsTek, Inc., 2013.
2 W. G. Coors, in *Advances in Ceramics - Synthesis and Characterization, Processing and Specific Applications*, ed. C. Sikalidis, InTech, 2011.
3 T. Norby, *Solid State Ionics*, 1999, **125**, 1-11.
4 E. Fabbri, D. Pergolesi and E. Traversa, *Chem. Soc. Rev.*, 2010, **39**, 4355-4369.
5 A. Unemoto, A. Kaimai, K. Sato, K. Yashiro, H. Matsumoto, J. Mizusaki, K. Amezawa and T. Kawada, *Solid State Ionics*, 2008, **178**, 1663-1667.
6 L. Yang, Z. Liu, S. Wang, Y. Choi, C. Zuo and M. Liu, *J. Power Sources*, 2010, **195**, 471-474.
7 G. C. Mather, D. Poulidi, A. Thursfield, M. J. Pascual, J. R. Jurado and I. S. Metcalfe, *Solid State Ionics*, 2010, **181**, 230-235.
8 A. Magrasó, C. Frontera, A. E. Gunnæs, A. Tarancón, D. Marrero-López, T. Norby and R. Haugsrud, *J. Power Sources*, 2011, **196**, 9141-9147.
9 K. D. Kreuer, *Annu. Rev. Mater. Res.*, 2003, **33**, 333-359.
10 S. Ricote, N. Bonanos and G. Caboche, *Solid State Ionics*, 2009, **180**, 990-997.
11 K. Katahira, Y. Kohchi, T. Shimura and H. Iwahara, *Solid State Ionics*, 2000, **138**, 91-98.
12 J. S. Fish, S. Ricote, F. Lenrick, L. R. Wallenberg, T. C. Holgate, R. O'Hayre and N. Bonanos, *J. Mater. Sci.*, 2013, **48**, 6177-6185.
13 D. A. G. Bruggeman, *Annalen der Physik*, 1935, **416**, 636-664.
14 R. Landauer, in *Electrical Transport and Optical Properties of Inhomogeneous media*, eds. J. C. Garland and D. B. Tanner, American Institute of Physics, 1978.
15 Z. Wu and M. Liu, *Solid State Ionics*, 1997, **93**, 65-84.
16 S. Kirkpatrick, *Rev. Mod. Phys.*, 1973, **45**, 574-588.
17 N. Bonanos, B. C. H. Steele and E. P. Butler, in *Impedance Spectroscopy Theory, Experiment, and Application*, eds. J. R. Macdonald and E. Barsoukov, John Wiley & Sons, Inc., Hoboken, NJ, 2nd edn., 2005, ch. 4, pp. 219-222.
18 D. H. Jeon, J. H. Nam and C.-J. Kim, *J. Electrochem. Soc.*, 2006, **153**, A406-A417.
19 P. Blennow, A. Hagen, K. K. Hansen, L. R. Wallenberg and M. Mogensen, *Solid State Ionics*, 2008, **179**, 2047-2058.
20 N. Bonanos, A Model for the Electrical Properties of Two-Phase Ionic Conductor Composites, Katarino, Bulgaria, 2011.
21 P. Blennow, K. K. Hansen, L. R. Wallenberg and M. Mogensen, *Solid State Ionics*, 2009, **180**, 63-70.
22 S. M. Sze, *Semiconductor Devices: Physics and Technology*, John Wiley & Sons Ltd, New York, 1985.
23 S. Jiang and J. B. Wagner, *J. Phys. Chem. Solids*, 1995, **56**, 1113-1124.
24 N. Sata, K. Eberman, K. Eberl and J. Maier, *Nature*, 2000, **408**, 946-949.
25 J. Schoonman, *Solid State Ionics*, 2003, **157**, 319-326.
26 J. Maier, *Physical Chemistry of Ionic Materials*, John Wiley & Sons Ltd, England, 2004.
27 R. Waser and M. Aono, *Nat. Mater.*, 2007, **6**, 833-840.
28 J. Nelson, *The Physics of Solar Cells*, Imperial College Press, London, 2003.
29 A. Ohtomo and H. Y. Hwang, *Appl. Phys. Lett.*, 2004, **84**, 1716-1718.
30 N. Sato, Y. Harada, T. Terashima, R. Kanda and M. Takano, *Appl. Surf. Sci.*, 2005, **244**, 588-592.

31 J. C. C. Abrantes, J. A. Labrincha and J. R. Frade, *J. Eur. Ceram. Soc.*, 2000, **20**, 7.

32 T. Tomio, H. Miki, H. Tabata, T. Kawai and S. Kawai, *J. Appl. Phys.*, 1994, **76**, 5886-5890.

33 S. Jiang and J. B. Wagner, *J. Phys. Chem. Solids*, 1995, **56**, 1101-1111.

34 T. Norby and R. Haugsrud, in *Nonporous Inorganic Membranes*, eds. A. F. Sammells and M. V. Mundschau, Wiley-VCH, Weinheim, 2006.

35 S. Ricote, A. Manerbino, N. P. Sullivan and W. G. Coors, *J. Mater. Sci.*, 2014, **49**, 4332-4340.

36 R. E. Williford, L. A. Chick, G. D. Maupin, S. P. Simner and J. W. Stevenson, *J. Electrochem. Soc.*, 2003, **150**, A1067-A1072.

37 D. Chen, Z. Lin, H. Zhu and R. J. Kee, *J. Power Sources*, 2009, **191**, 240-252.

38 W. Xing, G. E. Syvertsen, T. Grande, Z. Li and R. Haugsrud, *J. Membr. Sci.*, 2012, **415–416**, 878-885.

39 H. K. Bentzer, Ph.D. Thesis, Technical University of Denmark, 2010.

40 S. J. Song, E. D. Wachsman, J. Rhodes, S. E. Dorris and U. Balachandran, *Solid State Ionics*, 2004, **167**, 99-105.

41 S. J. Song, E. D. Wachsman, J. Rhodes, H. S. Yoon, K. H. Lee, G. Zhang, S. E. Dorris and U. Balachandran, *J. Mater. Sci.*, 2005, **40**, 4061-4066.

42 E. Vøllestad, C. K. Vigen, A. Magrasó and R. Haugsrud, *J. Membr. Sci.*, 2014, **461**, 81-88.

43 M. Liu, W. Sun, X. Li, S. Feng, D. Ding, D. Chen, M. Liu and H. C. Park, *Int. J. Hydrogen Energy*, 2013, **38**, 14743-14749.

44 S. J. Song, J. H. Moon, T. H. Lee, S. E. Dorris and U. Balachandran, *Solid State Ionics*, 2008, **179**, 1854-1857.

45 S. Escolástico, C. Solís, C. Kjolseth and J. M. Serra, *Energy Environ. Sci.*, 2014, **7**, 3736-3746.

46 R. Moos and K. H. Härdtl, *J. Am. Ceram. Soc.*, 1997, **80**, 2549-2562.

Table of Contents Entry

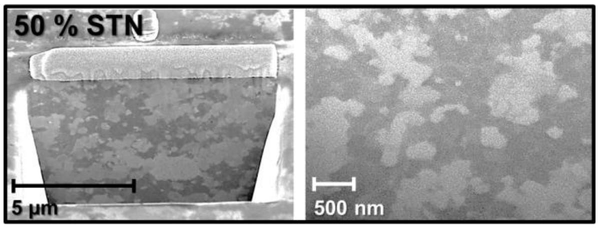

Dual-phase ceramic composite hydrogen separation membranes are synthesized by spark plasma sintering. The electrical properties and hydrogen flux performance are evaluated, suggesting promise for this unique composite material.